




Havriliak-Negami and Bergman type of dielectric response, together with Dyre's Hopping tunneling through random free energy barriers in $(\text{BiFeO}_3)_{0.8}$ — $(\text{CaTiO}_3)_{0.2}$ distorted crystalline structure

Santanu Sen^{1,*} , R. K. Parida², and B. N. Parida¹

¹Department of Physics, Central Institute of Technology Kokrajhar, (Deemed to be University, MoE, Govt of India) BTR, Kokrajhar, Assam 783370, India

²Faculty Of Engineering and Technology, Department of Physics, ITER, S'O'A Deemed to be University, Bhubaneswar, Odisha, India

Received: 30 March 2023

Accepted: 18 July 2023

Published online:

3 August 2023

© The Author(s), under exclusive licence to Springer Science+Business Media, LLC, part of Springer Nature 2023

ABSTRACT

An inter hexagonal species structural phase transformation from R3c to R3cH was found while doping BFO with 20% concentration of (CaTiO_3) , which manifests itself as distorted trigonal symmetry. The XPS analysis reveals dual oxidation states (Fe^{2+} & Fe^{3+}) of the $\text{Fe}2p_{3/2}$ state when deconvoluted. The existence of dominating O_{ads} is also confirmed, thereby giving a helping hand toward hopping and double exchange mechanisms. The permittivity curves followed both symmetric and asymmetric dispersion of relaxation mechanisms, which is best fitted by the Havriliak-Negami functions. The decrement of dielectric relaxation times with thermal energy validates the possibility of temperature-mediated induced entropies and phase lags of dipolar moments. The modulus dispersions curves were fitted following R. Bergman's formalism, which showed that the dielectric relaxations can be explained as a sum of some Kohlrausch-Williams-Watt β_{KWW} stretched exponents. The extracted numerics of β_{KWW} parameters proved the upper hand of dipolar interactions toward polarizability. The possibility of wider grain wall formation is also validated by it. The ferroelectric and magnetic studies revealed enhancement in the suppression of ferroelectric leakages relative to the parent composite and improved opening of M-H loops, reinforced by enhanced DM hamiltonian interactions due to structural bending and elongation in the double exchange interaction chain, together with the G-type antiferromagnetic phase of the host. The conductivity data fitting was performed by incorporating Dyre's RFEBM(Random Free Energy Barrier Model) model, where conductivity was verified to be following the mechanisms of hopping jumps through an extended range of free energy barriers.

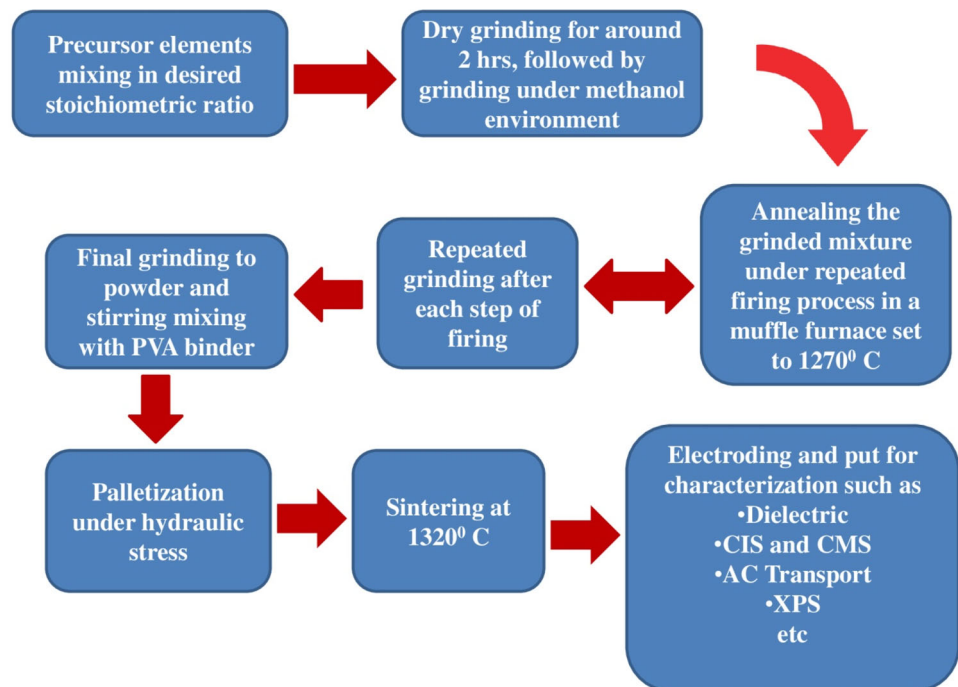
Address correspondence to E-mail: santanuphyaus@gmail.com

1 Introduction

BFO has been identified in its many forms and manifestations, viz hexagonal, rhombohedral, or pseudo-cubic phases, with the most commonly known [111]rh direction polarization moments arrangement capacity, although with low polarization retentivity and extended leakage transport [1, 2]. The limitation imposed by a higher leakage degree not only suppresses electrical polarizability but also reduces the magneto-electric coupling scopes [3]. The low canted angle depression between Fe ions on either side of $\langle 111 \rangle$ planes of pure BFO motif also has some limitations toward magnetic moments interaction capacity, which only backs anti-ferromagnetism and possibly some very feeble ferromagnetism. The only possible way to elevate its response is to dope or modify it with alkaline earth/rare earth or other transition class elements or structures bringing in improved ferroelectric, magnetic, and magneto-electricity interactions by means of structural distortions, exchange paths, improved charge balance and thereby suppressing leakage conductivity [4]. However, such modifications must be done at the cost of the disorderliness of the lattice, and glass-forming phases are thereby inevitable [5]. One such possibility was tried with Co^{3+} doping at the mid-octahedral location of BiFeO_3 , by Liang Bai et. al. [6] as $\text{BiFe}_x\text{Co}_{1-x}\text{O}_3$, evolved by incorporating the sol-gel path, having x magnitudes considered in odd interval step sizes as $x = 0.01, 0.03, 0.05, 0.07,$ and 0.10 . The expectation behind such a trial was to obtain an improved magnetic response in the ceramic. Magnetic measurements via VSM revealed that the M_r of $\text{BFCO}_{0.07}\text{O} \sim 3.6 \text{ emu cm}^{-3}$ with M_s strength of $\text{BFCO}_{0.10}\text{O} \sim 48.84 \text{ emu cm}^{-3}$. The results have seen comparatively twice the R-T strengths of pure BFO counterparts. $\text{Bi}_{1-x}\text{Sm}_x\text{FeO}_3$ nanoparticles, in the Sm_x concentration sweep of $0.05, 0.10, 0.15,$ and 0.20 were systematically produced and analyzed. The morphotropic phase boundary (MPB) was observed to be composed of a rhombohedral, orthorhombic interim $\text{Pna}2_1$ phase, alongside an orthorhombic phase in the x domain of $0.1 \leq x \leq 0.2$ was confirmed by crystallographic diffraction. Low-hysteresis loss featuring wasp-waisted magnetic loops was recorded, useful for multiferroic utilities [7]. The recent analysis focused on the elastic and anelastic traits of a BiFeO_3 – $\text{CaFeO}_{2.5}$ family of BCFO, which usually possess multiple instabilities, and were subjected to resonant

ultrasound spectroscopy. Some degrees of strain-induced expected ferroelectric-magnetic coupling were expected and thus were observed too, with localized strains significantly having a suppression effect on spin modulation [8]. The Mn doping-induced structural transition and vacancy inductions were analyzed on sol-gel prepared $\text{BiFe}_{1-x}\text{Mn}_x\text{O}_3$ (x as 0 to 0.05) thin films. A lifted bandgap of $E_g \sim 2.68 \text{ eV}$ was obtained in BCFMO film relative to BFO film, where E_g is $\sim 2.58 \text{ eV}$ [9]. A series of Pr-Cr co-doped BFO NTs as $\text{Bi}_{0.9}\text{Pr}_{0.1}\text{Fe}_{0.9}\text{Cr}_{0.1}\text{O}_3$ were grown on Anodic Aluminium Oxide (AAO) substrate having a pore diameter $\sim 250 \text{ nm}$ via by wet chemical liquid phase deposition approach. Significant breakdown of spin modulation together with strong magneto-dielectric behavior was noted in doped BFO NTs. The improvement of permittivity magnitudes was noticed, with respect to the increase in the applied magnetic field. The co-doped BFO nano-tubes exhibited notable increments in the MD magnitudes at a lower field sweep ($1\text{--}2 \text{ kOe}$) [10]. Sol-gel processed pure phase transition element (Mn, Cr) doped BiFeO_3 nano-particles were obtained. The determined band gap values were obtained as $1.92, 1.66,$ and 1.54 eV for pure, $5\% \text{ Mn},$ and $5\% \text{ Cr-doped}$ BiFeO_3 nanoparticles, respectively. The permittivity was observed to be increasing with transition elemental doping. The alternating field transport mechanisms were also found to be elevated [11]. Non-CS BFO, $\text{Bi}_{0.95}\text{Zr}_{0.05}\text{FeO}_3$, and $\text{Bi}_{0.95}\text{Dy}_{0.05}\text{FeO}_3$ thin films were spin-coated on $\text{Pt}/\text{TiO}_2/\text{SiO}_2/\text{Si}$ substrates and were analyzed for optical, and magneto-electric behavior. The results showed improved ferroelectric to magnetic response, where the Zr co-substitution was selected to be the best choice out of the other one [12]. Tg-DTA, structural transitional studies were undertaken on Ho and Nd doped BFO multiferroics, together with electrical and magnetic improvements were seen to be dominating [13]. BF-xCT nanoparticles were prepared via the sol-gel pathway in the extended ingredient range of $0.1 \leq x \leq 0.6$. Higher CTO modifier range viz $0.3 \leq x \leq 0.6$ resulted in orthorhombic (Pbnm) phase transformation for BFO, together with tapering of the optical gap. Some degrees of latent magnetization release were also seen in the remanence values of magnetization [14]. The intervention of CaTiO_3 (CTO) on permittivity and leakage transports of the polycrystalline BiFeO_3 (BFO) ceramics were thoroughly looked into. $(\text{BFO})_{(1-x)}\text{-(CTO)}_x$ disordered solution

Scheme 1 Schematic depicting experimental steps



with x as 0.6, 0.7, and 0.8 were sintered through direct mixing of the calcined powders. Improved permittivity dispersions and low tangent dissipation were novel findings [15]. As per earlier findings, the sequential appearance of tetragonal symmetry in the BFO lattice may also be attributed to the Jahn–Teller symmetric/anti-symmetric elongating and buckling distortions brought in the of Mn^{3+} substituted $(\text{Fe})^{3+}\text{O}_6$ [16, 17]. Following the immense possibilities of enhancing the physiological character and identities of BFO by mere doping or modification of its structure, going through such previous reports always keeps the door open for various other trials and here in this work too we are carrying forward that trial again.

2 Composite processing and analysis tools

2.1 The distorted crystalline structure synthesis pathway

The solid solution was formed as dry calcined powder following the high thermal energy-assisted reaction among 0.4 Bi_2O_3 , 0.4 Fe_2O_3 , 0.2 CaCO_3 , 0.2 TiO_2 precursors to finally form the glass former as 0.4 Bi_2O_3 + 0.4 Fe_2O_3 + 0.2 CaCO_3 + 0.2

$\text{TiO}_2 = (\text{BiFeO}_3)_{0.8}-(\text{CaTiO}_3)_{0.2}$, alongside the evolution of 20% of CO_2 . Initially, well before the heat treatment, the precursor compounds were dry and wet ground for quite well time to achieve the ideal grain sizes required for the fusion reaction purpose. The composite was then put under the cycle of recursive cycles of ignitions, in ideal step intervals of thermal energy increment, till reaching the sample forming temperature which in this case was around 1270 °C. After visual and crystallographic confirmation of sample conglomeration, the lump was further ground and mixed with binder solutions. Finally, palletization of the formed solid solution was done for further characterization. The entire aforementioned processes are enumerated in the form of an experimental Scheme 1.

2.2 Various analysis tools employed

2.2.1 X-ray diffraction (XRD)

Instrument specifications: RIGAKU, ULTIMA IV, 2 θ sweep of 20 $^\circ$ –80 $^\circ$.

2.2.2 XR-photoelectron spectroscopy

Instrument Specifications: ESCALAB Xi + , resolution degree of < 3 μm , capable of focusing x-rays on spots of diameter varying from 900 μm to 200 μm .

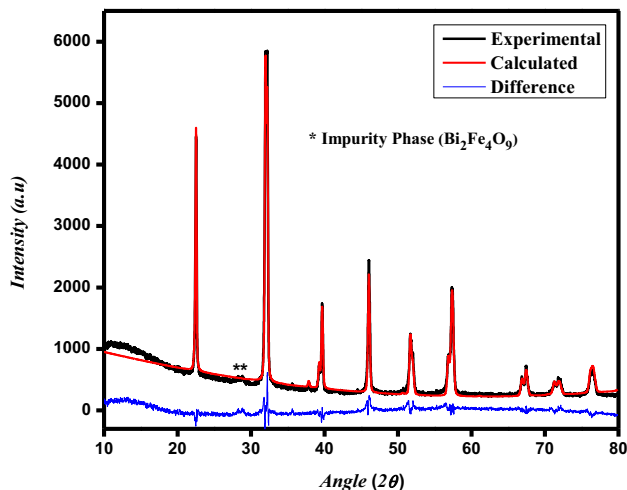


Fig. 1 The Rietveld fitted profile

2.2.3 Ultra violet-visible spectrophotometry

Instrument Specifications: Shimadzu-2600 UV spectrophotometer, absorbance based spectrophotometer, works in the 0.1 nm bandwidth, operates in the spectral sweep of 200 nm – 800 nm, assembled with a radiation scattering minimize- an integrating sphere (ISV-922) of 60-mm dimension.

2.2.4 Dielectric, modulus, and conductivity analyzer

Instrument Specifications: Low precision PSM 1735, N4L-LCR (UK origin), operated in the frequency range 100 Hz to 1 kHz, temperature step size of 2 °C.

2.2.5 P-E loop tracer

Instrument Specifications: Precision Multiferroic II Ferroelectric Tester (Radiant Technologies), unique built-in frequency rating of 270 kHz at ± 100 V, can capture 32,000 points at 2 MHz. Performed at R-T.

2.2.6 M-H loop magnetometry

Instrument Specifications: Lake Shore 8600 Series VSM, max fields to 3.1 T. Performed at R-T.

3 The investigation outcomes

3.1 The structural phase identification: XRD refinement

The refinement task was executed following the Rietveld approach on the experimental diffraction peaks (Fig. 1). A 1528378.cif file was employed as the reference XRD card for the refinement purpose, which was obtained from the Crystallographic Open Database. A transition from an orthodox R3c rhombohedral phase for pure BFO [18] or R3c hexagonal [19, 20] to a more unstable and distorted R3cH trigonal phase was achieved, belonging to the BFO hexagonal species. Any peak shifting relative to BFO characteristics peak [18–20] positions is either due to half or interstitial replacements. The tolerance factor evaluation by employing the expression

$$t.f = \left\{ \frac{(1-x)\langle Bi^{3+} \rangle + x\langle Ca^{2+} \rangle + \langle O^{2-} \rangle}{2} \right\} \left(\sqrt{2} \right)^{-1} \left\{ \frac{(1-x)\langle Fe^{3+} \rangle + x\langle Ti^{4+} \rangle + \langle O^{2-} \rangle}{2} \right\}^{-1}$$

Here the notations $\langle Bi^{3+} \rangle$, $\langle Ca^{2+} \rangle$, $\langle Fe^{3+} \rangle$, $\langle O^{2-} \rangle$ and $\langle Ti^{4+} \rangle$ denotes the respective ionic radii of the ingredient elements. The calculated magnitude of the tolerance factor (t.f) was 0.80, which gives an additional confirmation of perovskite phase formation, particularly manifesting as trigonal distortion. The Scherrer equation revealed the particle size as 71 nm belonging to the polycrystalline/glassy phase. The lattice translational parameters values are

Table 1 The trigonal system ionic positions

Ionic Terminology	x	y	Z
Bi1	0.01893211	0.02579409	– 0.0044714096
Ca1	0.01893211	0.02579409	– 0.0044714096
O1	0.43915275	0.006637733	0.95679843
Ti1	0	0	0.22233409
Fe1	0	0	0.22233409

Table 2 The most common structural bond angles

Chain	Ionic locations		Coordination + Coordinates expression			Angles (in degrees)
	Fe/Ti or Bi/Ca	O	Fe/Ti Or Bi/Ca	Ti1/Fe1 or Bi/Ca	O1	
Ti1/Fe1-O1-Fe1/Ti	1.00000	0.90082	0.66667	(1, 1, 0) + x, y, z	(1, 0, -1) + -x + y + 1/3, y + 2/3, z + 1/6	156.6
Fe1/Ti1-O1-Fe1/Ti	0.33333	0.23415	-0.0000	(0, 0, 0) + -y + 1/3, -x + 2/3, z + 1/6	(0, 1, -1) + -x + y + 2/3, -x + 1/3, z + 1/3	156.7
Bi1/Cal-O1-Bi1/Cal	0.38900	0.29013	0.22233	(0, 0, 0) + -y, -x, z + 1/2	(0, 0, 0) + -y + 1/3, x-y + 2/3, z + 2/3	113.1
Cal/Bi1-O1-Cal/Bi1	1.00686	0.99336	0.67353	(1, 1, 0) + -x + y, y, z + 1/2	(0, 0, 0) + -x + y + 2/3, -x + 1/3, z + 1/3	111.3

being $a = b = 5.552212 \text{ \AA}$ error: 3.9302537×10^{-4} , $c = 13.753269 \text{ \AA}$ error: 0.0011817557 , $V = 2080.6611$ error: 141.6731 \AA^3 . The refinement reliability parameters are $\text{sig} = 2.643775$, $\text{Rwp} (\%) = 11.497714$, $\text{Rwpnb} (\%, \text{ no bkg}) = 29.153008$, $\text{Rwpnb1} = 14.007998$, $\text{Rwpnb2} = 8.523347$, $\text{Rb} (\%) = 9.636416$, $\text{Rexp} (\%) = 4.348976$. The ionic positions were also evaluated and tabulated in Table 1. The secondary phase volume fraction numeric was found to be 0.031 error: 0.018. The micro-structural strain magnitude was also found from the result analysis as 0.0015658471 error: 5.0360984×10^{-5} . The bond angle (Bi/Ca-O-Bi/Ca, Fe/Ti-O-Ti/Fe) data tabulated in Table 2 among the neighboring pairs were seen to be more depressed, relative to BFO [21], confirming more distortions in the motif. The bond length data provide another support/backing to the statement of structural deformations, as shown in Table 3. A comparative findings on various other parameters alongside structural is tabulated in Table 4 on CTO modified BFO motifs.

3.2 The X-ray photoelectron spectra

The XPS analysis is a reliable technique to analyze in detail the diversity of the elemental valencies and atomic percentage concentrations in the formed complex. It not only clarifies the presence of the supposed ingredients of the glass former but also validates the possibility of any possible exchange interaction between short or long-range chains of ferroelectric and ferromagnetic pathways. Such a detailed analysis survey scan plot alongside the spin-orbit interaction affected, degeneracy removed fine spectral peaks for all the possible compositional candidates are depicted in Fig panel 2a–g. The survey scans [2(a)] in the entire possible B.E. sweep show sharp elemental orbital peaks, with their present atomic percentages. The finer S–O interaction fine peaks belonging to Bi4f, Fe2p, and Ti2p (Fig. 2b–d) are shown with their corresponding B.E. peak location coordinates. The inspection for the existence of some possible multiple transition element valency states was performed via Gaussian deconvolution. The Fe2p_{3/2} (Fig. 2c, e) peak was found to be containing two inner peaks corresponding to the traditional B.E. magnitudes as reported earlier on similar composites [22, 23]. It was identified that the Fe²⁺ state valency concentration is quite high. The Fe2p_{3/2} eigenstate Fe³⁺ to Fe²⁺ percentage concentration ratio

Table 3 Some common bond lengths

Channel	Atomic positions		Coordination + Coordinate Expressions		Bond length (in Å)	
	Bi/Ca or Fe/Ti	O	Bi/Ca or Fe/Ti	O		
Bi/Ca- O	0.68560 0.32886	0.35913 0.29013	1.10582 0.33997	$(0, 0, 0) + x + 2/3, y + 1/3, z + 1/3$	$(0, 0, -1) + x + 2/3, y + 1/3, z + 1/3$	2.43
Ti/Fe- O	1.00000 0.22233	0.00000 0.29013	1.10582 0.33997	$(1, 0, 0) + x, y, z$	$(0, 0, -1) + x + 2/3, y + 1/3, z + 1/3$	1.92

Table 4 Comparative data with other results of the CTO doped BFO

Composite	Lattice Distortion	E_g in (eV)	M_r (emu/gm), M_s (emu/gm)	2Pr (μCcm^{-2})
(BiFeO ₃) _{0.6} (CaTiO ₃) _{0.4} [22]	Orthorhombic[Pbnm (c, a, b)]	1.85	0.061, ≈ 0.425	≈ 0.1192
(1 - x)BiFeO ₃ - xCaTiO ₃ (BF-xCT) [14]	Rhombohedral (R3c) for $0.1 \leq x \leq 0.2$ and orthorhombic (Pbnm) for $0.3 \leq x \leq 0.6$	1.96–2.25	≤ 0.112 , Unsaturated	Not reported
0.8BiFeO ₃ -0.2CaTiO ₃ (0.8BFO-0.2CTO) [64]	Rhombohedral structure (space group R3c)	2.26	Not reported	Not reported
(Bi _{1-x} Ca _x)(Fe _{1-x} Ti _x)O ₃ [65]	Rhombohedral R3c ($x \leq 0.2$) to orthorhombic Pbnm ($x \geq 0.3$)	Not reported	~ 0.18 , Unsaturated	~ 0.56
Present composite	Trigonal (R3cH)	1.74	0.1675, 0.4903	~ 0.464

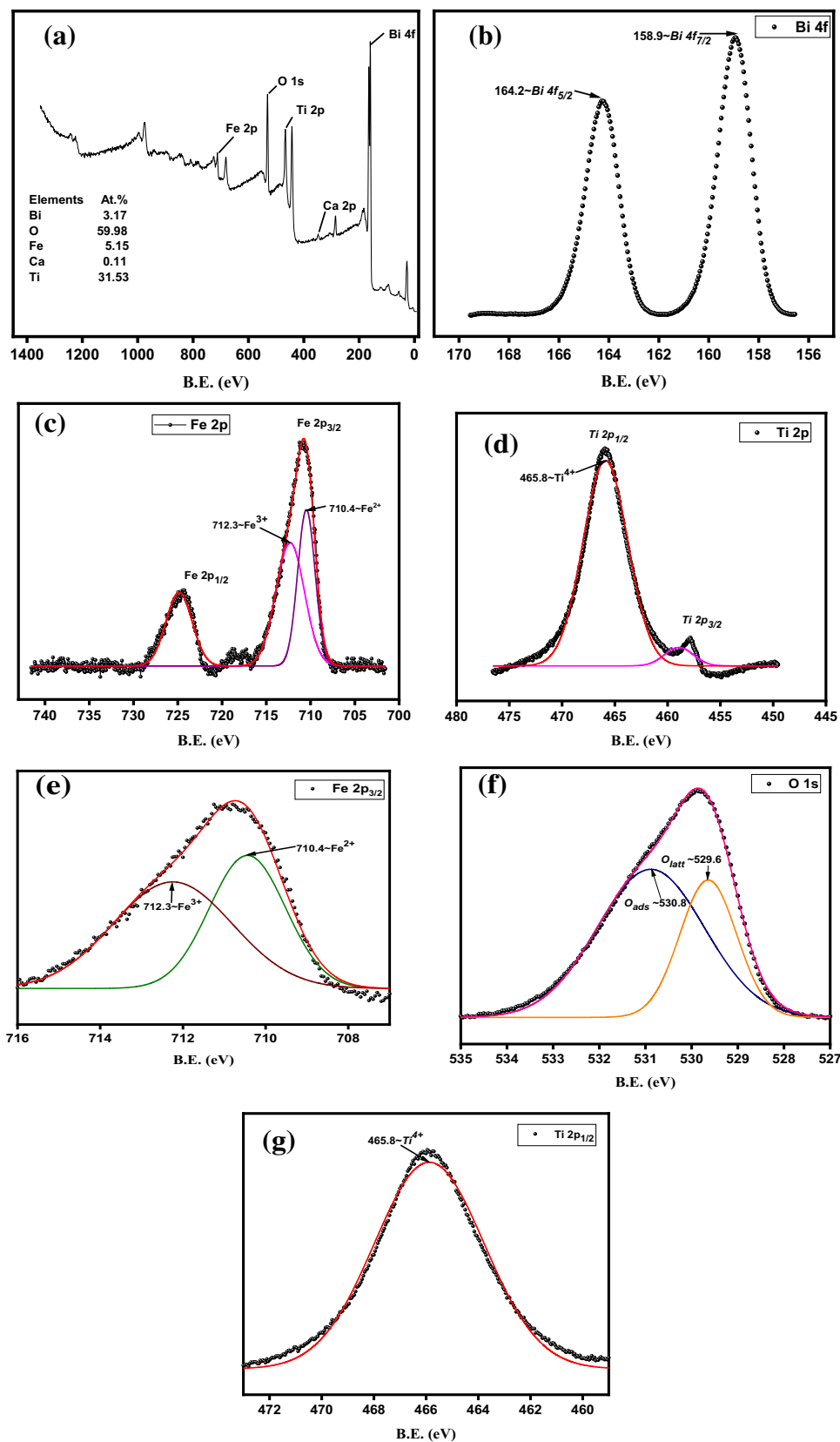
is 55.64%:44.35%. Such findings confirm the existence of back-and-forth polaron hopping paths among Fe²⁺ and Fe³⁺. Such an assumption was further clarified when the O1s state was deconvoluted. The O1s state deconvolution (Fig. 2f) immediately clarified the reason behind the dominance of the Fe²⁺ state, since the O_{ads} peak area was seen to be larger. This necessitates a short/long spread hopping path chain and an exchange path existence. The required composite neutrality is also ensured by it. The Ti2p_{1/2} deconvolution Fig. 2g though tells a different story since it gives only single peak deconvolution belonging to the majority of Ti⁴⁺ states, unlike previous reports [22, 23]. Hence it can be confirmed that titania substitution has little role to play in the interaction mechanisms and it also ensures the correct octahedral substitution of Ti.

3.3 The optical band gap evaluation through UV-visible

The optical transition energy gap was estimated from the ambient conditional UV analysis. The absorbance spectral plot (Fig. 3a) lies within a wavelength sweep of 50–850 nm. The maxima of the absorbance peak were identified at the 443 nm wavelength location,

which might be an indication of carrier transition among the O2p state of VB and Fe3d of CB [24]. The Tauc plot was extrapolated to find an approximate estimation of the optical direct transitional gap, which is the relation $[\alpha hv]^{\frac{1}{2}} = A [hv - E_g]^{\frac{1}{2}}$. The absorption coefficient is evaluated by employing the relation $\alpha = 2.303A$, where A stands for absorbance of the sample. The plot is essentially among (αhv) along the y-axis and hv energy quantas along the x-axis, which when extrapolated for $\alpha = 0$ on the x-axis gives us the optical band gap E_g . The resulting value of the optical band gap was observed to be 1.74 eV, from the taut curve (Fig. 3b) which is less relative to previously reported findings [14]. Such narrowed-down optical band gap is a direct consequence of the excess oxygen vacancies, visible from XPS deconvolution data. The presence of occupied 2p adsorbed oxygen band in between the CB and VB lifts up the donor level and donor defect levels gets close to the conduction band (Shallow donor). Also, Reduced oxygen atoms or a lower coordination number (Z) are the definitions of oxygen vacancy. The relationship between band width, the hopping integral and coordination number is straightforward. $B = KTZ$, the band width. K is the proportionality constant and T is the integral of hopping. Thus, oxygen vacancy

Fig. 2 a–g The XPS Profiles



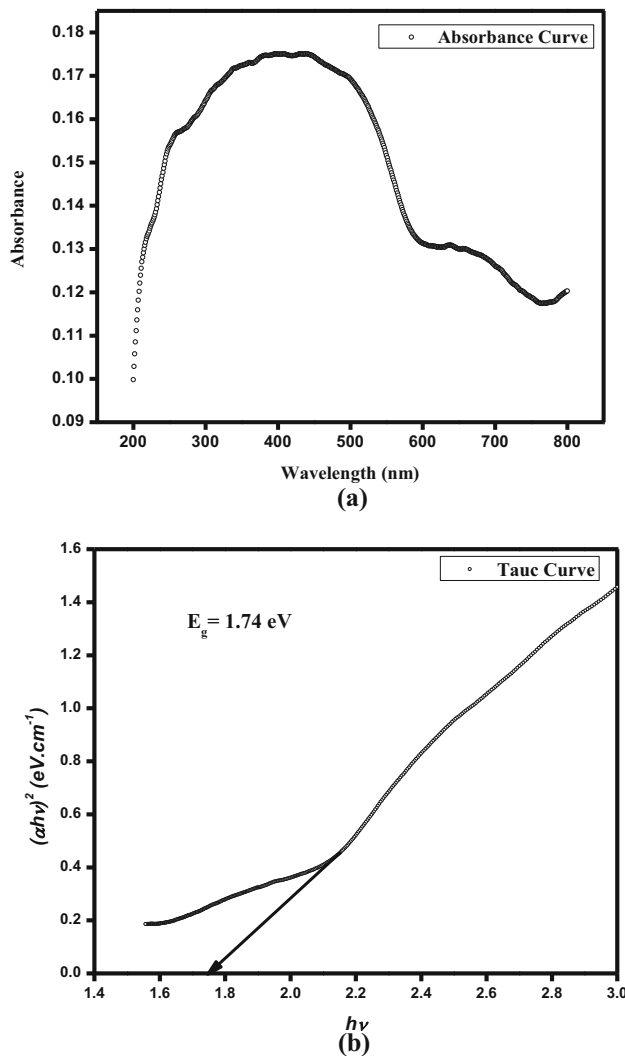


Fig. 3 **a** The Absorbance Plot. **b** Tauc Plot

may cause the band width (B) to narrow. The structural distortion, which is also a deciding and influencing factor toward optical gap lessening is playing a role here, as confirmed by the structural distortion verifying parameters such as volume fraction, bond length, and bond angle data.

3.4 The Havriliak-Negami type of dielectric dynamics

The thermal dependency dielectric dispersion and relaxation times are quite often observed with disordered solids or glass-forming composites. Alongside, mixed dispersion and relaxation non-debye behavioral dynamics with such systems are quite common with inter and intra-cluster short-range atomic and polaron transport [25]. Hence unlike

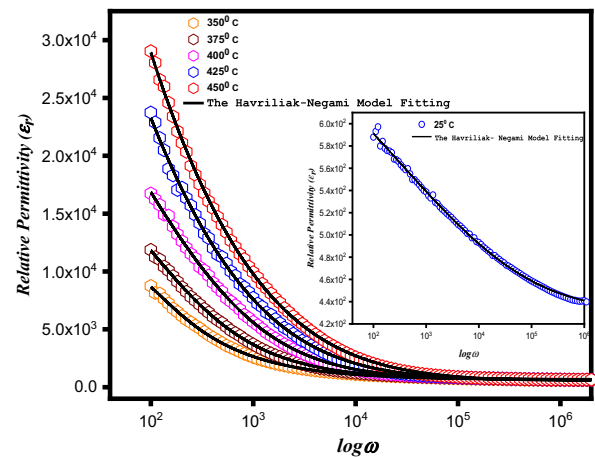


Fig. 4 The Havriliak-Negami fitted permittivity profile

Debye or Cole–Cole formalism, a dual (symmetric and asymmetric) dispersion mechanism-dependent formalism was devised to explain such complex permittivity response, which was again temperature dependent. Such a mechanism is known as the Havriliak-Negami (H-N) model [26, 27]

$$\epsilon_r(\omega) = \frac{\epsilon_r(h.f.)[1 + (i\omega\tau_r)^{1-\lambda}]^\delta + [\epsilon_r(static) - \epsilon_r(h.f.)]}{[1 + (i\omega\tau_r)^{1-\lambda}]^\delta}$$

also expressed as the superposition of some stretched exponential functions, known universally as Kohlrausch–Williams–Watts (KWW) functions [28–30]. Here $\epsilon_r(h.f.)$, $\epsilon_r(static)$ are the high and low frequency span permittivity, τ_r being the relaxation time, λ the width of the H-N relaxation period spread, and δ the measure of H-N asymmetry of relaxation time spread. The fitting of the dielectric permittivity data so obtained has been performed successfully following the aforementioned relation, as depicted in Fig. 4 and the data of the extracted H-N parameters were tabulated (Table 5) A quick inspection of the extracted dielectric parameter data reveals that the relaxation times (τ_r) times keep on exhibiting a magnitude-reducing trend with temperature increments. Such an outcome is a direct indication of the enhanced thermal orientation entropy of the permittivity moments. Both symmetric as well as asymmetric dispersion parameters (λ, δ) exhibit thermal enhancement in their values, thereby further confirming the enhanced phase lag of the polarization moments, induced by temperature increment. The increased magnitude of the low-frequency static moments relative to temperature directly signifies the

Table 5 The HN dielectric fitting parameters

Temp °C	$\epsilon_r(\text{static})$	$\epsilon_r(\text{h.f.})$	τ_r	$1 - \lambda$	δ
25(R-T)	769.52727 ± 95.10061	432.2085 ± 4.82282	2.90218E-7 ± 5.10056E-6	0.19784 ± 0.08913	0.01856 ± 0.00305
350	11,886.17781 ± 1369.07754	635.39634 ± 9.24287	0.01389 ± 0.00222	2.16224 ± 0.5284	0.30245 ± 0.07752
375	22,193.82571 ± 1986.10839	656.81897 ± 10.03101	0.01194 ± 6.14424E-4	0.89048 ± 0.10307	0.84841 ± 0.12069
400	46,219.72049 ± 5503.34992	676.95904 ± 14.93102	0.00364 ± 0.00132	0.46916 ± 0.05515	2.13755 ± 0.42995
425	226,589.80034 ± 189,287.87452	628.37673 ± 45.5861	1.9556E-4 ± 0.00136	0.22161 ± 0.10748	6.58323 ± 8.58769
450	336,427.32416 ± 227,153.71945	536.63741 ± 44.62982	5.06143E-4 ± 0.00231	0.20859 ± 0.07666	5.75022 ± 4.94569

magnified field phase synchronized short-range polaron hopping, defect concentration increment, and transition ion valency fluctuations, which can be directly perceived from the XPS data. The h.f. permittivity parameters are fixed magnitude saturated, at nearly the same magnitudes for all discrete selected temperatures. The tangent loss plot (Fig. 5) quite expectedly displays comparative behavior, with proof of strong magnitudes of freeze-out polarizabilities, particularly at low-range frequencies. However, the magnitudes of low frequency loss strengths are very low, even at considerably high temperatures. The long-range polaron leakage conductivity becomes an evident and dominant factor as tangent loss saturates at high frequency spread. Increasing slopes of tangent curves with discrete temperatures suggest elevated oxygen vacancy tangled hopping polarization chains between ferrite multiple valency states.

3.5 Bergman dielectric modulus

A few earlier reports [31, 32] established a relative connection between HN dispersion parameters and the KWW stretched functional parameters. The $\beta(KWW)$ correlation and interaction term (the stretching factor) is somewhat closely entangled with the asymmetric and symmetric H-N dispersion parameters, particularly in clustered dipolar glass-formed ceramic oxide complexes [33]. Hence, R. Bergman [34] devised a frequency domain theoretical model to describe the dipolar quasi-ferroelectric relaxor behavior, in terms of complex modulus response, under the expression-

$$M''(\omega) = M''_{peak} \left[(1 - \beta_{KWW}) + \left(\frac{\beta_{KWW}}{1 + \beta_{KWW}} \right) \left[\beta_{KWW} \left(\frac{\omega_{peak}}{\omega} \right) + \left(\frac{\omega}{\omega_{peak}} \right)^{\beta_{kww}} \right] \right]^{-1}$$

The experimental curves of M'' vs logarithmic frequencies (Fig. 6) were fitted by employing the aforementioned expression. The best-converged fit of the theoretical Bergman model with the data curves deconvolutes the temperature variant numeric values of the Bergman fitting parameters such as relaxation frequency ω_{peak} , M''_{peak} and of course the correlation stretching Kohlrausch-WW β term. A traditional linear behavior of the β factor against increasing temperature [35] can be observed in Table 6 and Fig. 7. Its

magnitude was observed to be lying within its standard universal limit $0 < \beta_{KWW} \leq 1$, for extensively disordered glassy systems. This also implies that the dipoles accumulated along grain walls are strongly coupled [36], confirming non-debye relaxations. Such interactions are a direct consequence of the wide grain wall width and crowded dipolar densities. Since β_{KWW} magnitudes are increasing and tend toward unity, it directly implies that the dipolar interactions are slowly reducing with thermal energy increments, although remaining a dominating factor. This also explains why the relaxation times have a declining trend with temperature in M'' fitting results. The enhancing trend of the M''_{peak} values signifies temperature-mediated weakening of the capacitance (since $M''_{peak} \propto C^{-1}$ [37]) of the solid composite, the reason for which is the weakening of the dipolar moment interaction. The activation energy $E_a = 2.06eV$ was estimated from the slope of $\ln \tau_M$ and $10^3/T$ K^{-1} plot (Fig. 8), making utilization of the Arrhenius relation. The frequency relative M' curves (Fig. 9) ensures electrode effect suppression, hopping effect stretched dispersion, and mobility, as the curves possess some saturation tendency at maximum frequency limits [37–41].

3.6 Z' and Z'' arcs (The Nyquist plot)

The inspection of bulk, grain wall, and electrode between grains and glass former to electrode interface can be performed from the study of relaxation

arcs from Z' vs Z'' plot, also known as the Nyquist plot approach. Usually, for the type of solid complex under investigation, the semicircular arcs obtained from the Nyquist analysis are such that their center lies off the real impedance, Z' axis [42] because of the porous and non-ideal tight-packing of the grains. This, as a consequence, brings in some non-ideal capacitive response along the interfaces and hence the parallel C-R circuit inherently requires a complex constant phase adjusting element (CPE) in parallel for the adjustment requirement of the relaxation frequency [43–48]. Various configurations of equivalent Randle networks, involving R_{bulk} , C_{bulk} , $R_{grainwall}$, $C_{grainwall}$, and Q_{CPE} are being incorporated to theoretically best fit the arcs, considering the non-debye type of relaxations at various temperatures as shown in Fig. 10a, b. The overall complex impedance response of the solid solution may be expressed as

$$Z(\omega) = R_{bulk} + \frac{1}{(R_{grainwall})^{-1} + \left(\frac{1}{C_{grainwall}(i\omega)}\right)^{-1} + \left(\frac{1}{\rho(i\omega)^\eta}\right)^{-1}}$$

The ρ term is the CPE element $\frac{1}{\rho(i\omega)^\eta}$, whose nature depends on the exact value η . Under the debye relaxation category, CPE is an ideal capacitance element for which the value of η being equal to unity. Whereas, for CPE to be an ideal resistive component, the value of η being equal to zero [49]. The fitting performance was observed to be quite satisfactory, with the delineation of single bulk effect arcs in the relatively low-temperature range (300°–375°) C, after which a small semicircle, like a kink, is observed,

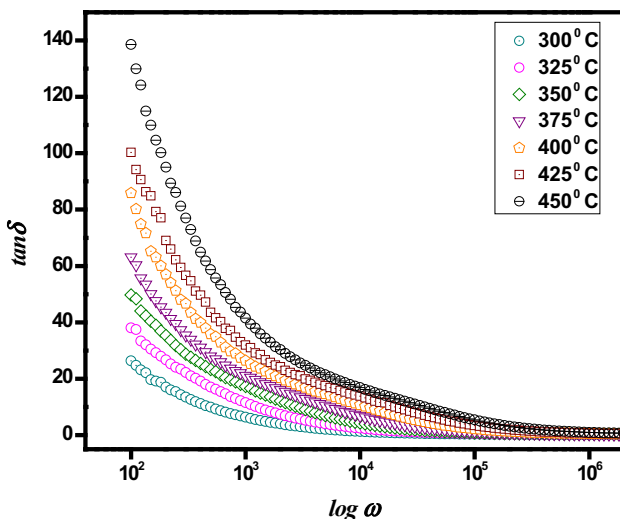


Fig. 5 The Tangent delta dissipation

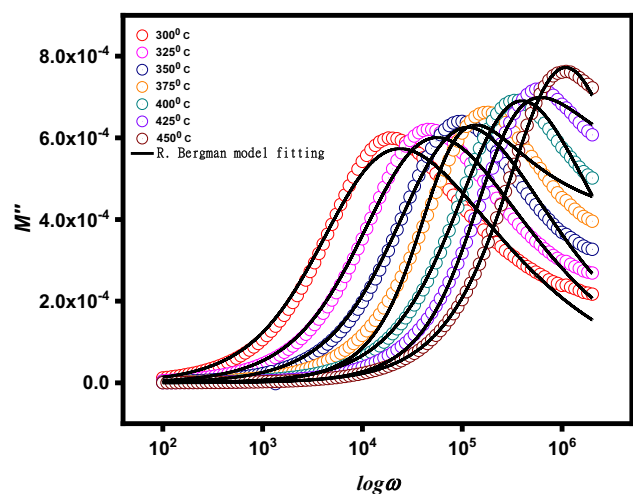


Fig. 6 The M'' curve fitting employing R. Bergman Model

Table 6 The various modulus fitting extracted parameters

Temp °C	ω_{peak}	β_{KWW}	M''_{peak}
300	23,835.67779 ± 511.37981	0.50914 ± 0.007	5.73425E-4 ± 5.17044E-6
325	56,045.98997 ± 950.15434	0.54153 ± 0.0068	6.00697E-4 ± 4.57269E-6
350	114,233.97878 ± 1616.87608	0.5758 ± 0.00703	6.25659E-4 ± 4.21524E-6
375	137,689.412 ± 4200.20046	0.6242 ± 0.01914	6.31261E-4 ± 6.23353E-6
400	397,176.53673 ± 3480.0718	0.63903 ± 0.00641	6.90593E-4 ± 2.76604E-6
425	613,984.76946 ± 12,821.21099	0.68158 ± 0.00867	6.98886E-4 ± 2.47562E-6
450	1,086,374.00807 ± 6780.68497	0.73114 ± 0.0048	7.72222E-4 ± 1.14476E-6

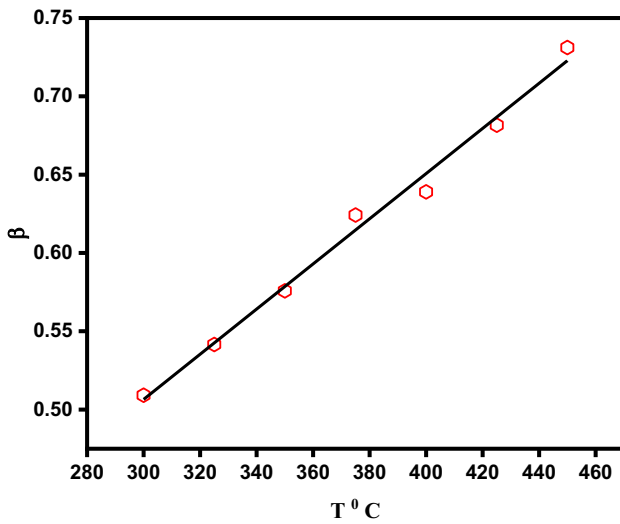


Fig. 7 Linear traditional temperature variation of β_{KWW} exponent

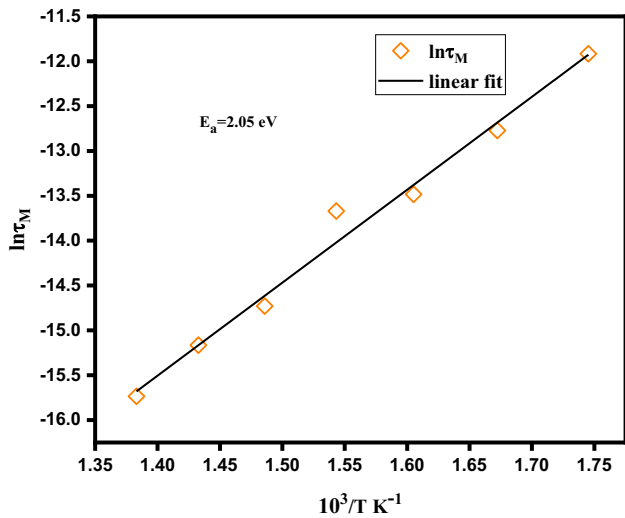


Fig. 8 The $\ln \tau_M$ vs $10^3/T$ K⁻¹

possibly due to grain wall effects. Such small radii of grain wall arc may be due to the reason that bulk and

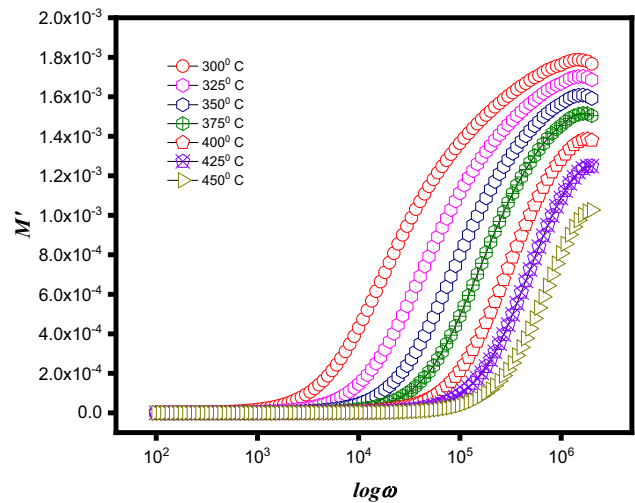


Fig. 9 M'' vs $\log \omega$

grain wall resistive contributions are equivalent. The reducing diameters of the arcs support the ntc response and semiconducting characteristics assumption. The intercept values for single semicircles as R_{bulk} were extracted and plotted as an Arrhenius plot as depicted in Fig. 11. The activation energy for bulk restive effects was then evaluated as being equal to 2.18 eV.

3.7 The RFEBM (Random Free Energy Model) for ac transport

A more realistic theoretical description of ac transport mechanisms in disordered systems such as the composite under investigation can be best described and fitted by Jeppe C. Dyre’s RFEBM model [50], $\sigma_{ac}(\omega) = \sigma_{dc}(0)\omega\tau \arctan(\omega\tau) \left\{ \frac{1}{4} \ln^2(1 + \omega^2\tau^2) + (\arctan \omega\tau)^2 \right\}^{-1}$ which based on the assumption that the activation energies for ac conductivity is quite less than the dc conductivity activation energy, which is more thermal energy dependent. The quadratic dependence of

ac transport on frequency as well as the temperatures implies that a wide sweep of activation energies is associated, considering the disorderliness of the solution. This empirical assumption is not that radical, considering some very early reported related assumptions [51, 52]. Hence the idea of hopping of quasi charges, as thermally activated jumps through a distribution of free energy barriers, $\Delta F = \Delta E - T\Delta S$ was assumed, where ΔE and ΔS corresponds to the energy and entropy barriers respectively. The $-eS$ barrier was supposed to be contributed from the tunneling process, which under the circumstances is proportional to the tunneling range. Considering all such possibilities, both ionic and electronic contributed transports are taken into the picture. Figure 12a, b are such plots against such log scale frequency and log scale ac transport, which is quite ideally fitted to the mentioned model. The R-T

conductivity curve as portrayed in Fig. 12a directly proves the temperature dependence of dc transport since at low temperature, the dc transport part is almost negligible and ac conduction plays dominant role with frequency. As thermal energy enhances, the prominence of the low frequency domain $\sigma_{dc}(0)$ transport is visible, with barrier hopping becoming prominent at higher frequencies.

3.8 Inspection of multiferroic phases

3.8.1 The ferroelectric phase (P-E Loop Trace) analysis

The first-hand confirmation of the presence of multiple ferroic orders in the same phase can be confirmed from the outcomes of the P-E hysteresis loop trace. The experimentally obtained onset plot of the ferroelectric response is recorded in Fig. 13. The genesis of ferroelectricity in BFO is the contribution coming from the lone pair $6s^2$ orbital residing electrons belonging to Bi^{3+} ions. However, the width of the P-E loop for pure BFO is very thin since the contribution toward polarizability by pure BFO is very weak as its transport capacity is quite large [53]. On the other hand, mixed BFOs are quite charge-balanced and show a widening of loops with varying doping concentrations. Unlike leaky transport and high coercivity characteristic of similar doped BFO oxides [54–56], the composite’s P-E loop shows low leakage and low magnitudes of coercivity ($E_c \sim 0.836 \text{ kVcm}^{-1}$). Thus a stabilized energy storage capable composite formation is being achieved. The

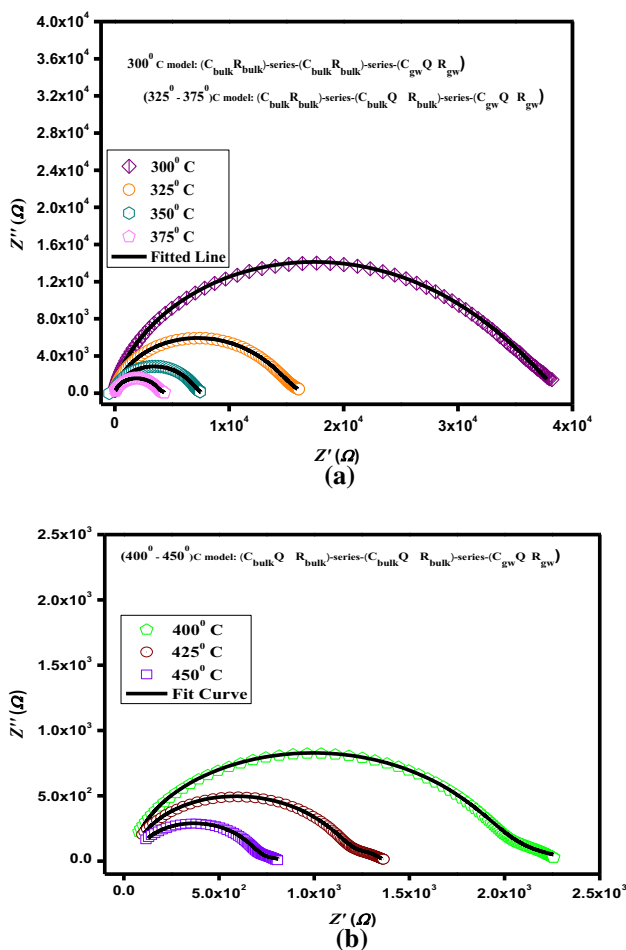


Fig. 10 a Nyquist plot in the temperature interval 300 °C–375 °C. b Nyquist plot in the temperature interval 400 °C–450 °C

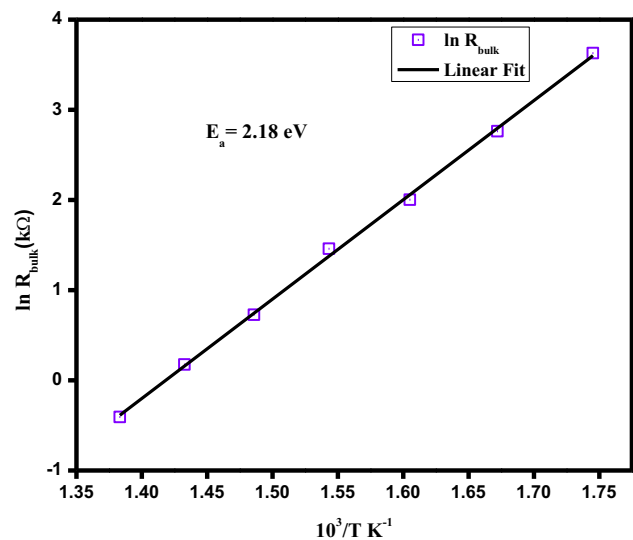


Fig. 11 The $\ln R_{\text{bulk}}$ against $1000/T \text{ K}^{-1}$

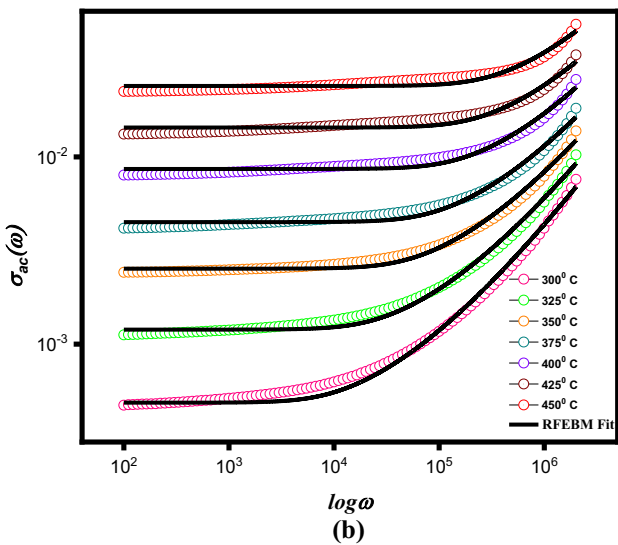
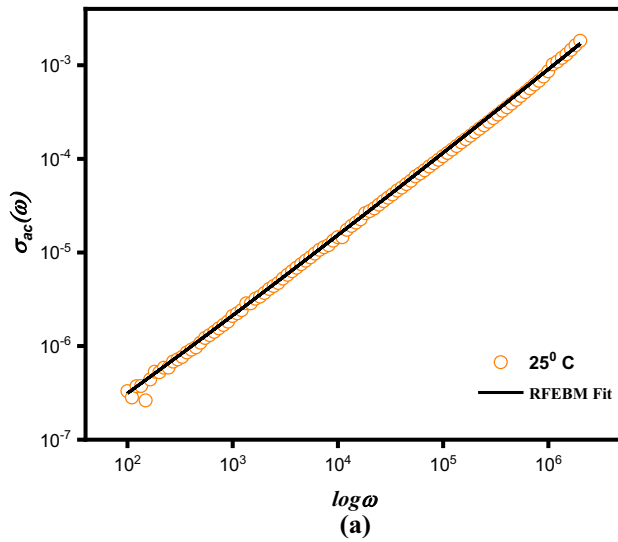


Fig. 12 a The RFEBM fit for room temperature conductivity. b The RFEBM fitted ac transport plot for elevated temperatures

$2P_r$ magnitude is of $\sim 0.464 \mu C cm^{-2}$ order which may be because of the improved ferroelectric response, originating from the suppression of the volatile nature of Bi by Ca substitution [57]. Also, any kind of structural distortions brought in by phase transformations, as observed, may be held accountable for enhanced ferroelectric strength [56].

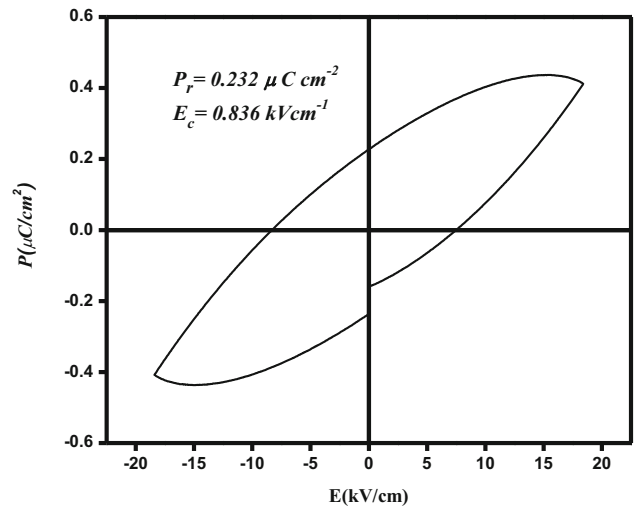


Fig. 13 The P-E trace at R-T

3.8.2 The weak ferromagnetism (M-H loop at the ambient condition)

The magnetic interaction in pure BFO is dominantly G- kind antiferromagnetic, due to modulated spin alignments [58]. This manifests itself as spin state interaction between exactly anti-parallel aligned moments of adjacent Fe ions. However, the adjacent magnetic moments of Fe ions are slightly less anti-parallel, due to the spin state anti-symmetric exchange mechanisms known as the DM (Dzyaloshinskii-Moriya) interactions among \hat{S}_i and \hat{S}_j magnetic spin states of adjacent Fe ions [59]. This effect produces some canting of bond angles, hence inducing some dominant degrees of the ferromagnetic loop as depicted in Fig. 14. The presence of low leakage ferroelectricity and thereby multiferroicity ensures magnetoelectric coupling alignments in the composite, which further backs the involvement of $H_{DM} = \tilde{D}_{ij}\{\hat{S}_i \times \hat{S}_j\}$ (DM) interactions, where symbols carry their identified meanings [60–63]. Thus this observation can point toward the existence of magneto-electric coupling orders in the solid glass former in an indirect way. It is needless to say that enhanced degrees of DM interactions cannot be realized if there are no resultant lattice distortions. The depressed values of bond angles among various B-site transition ion/A-site pairs, as shown in Table 2 is direct

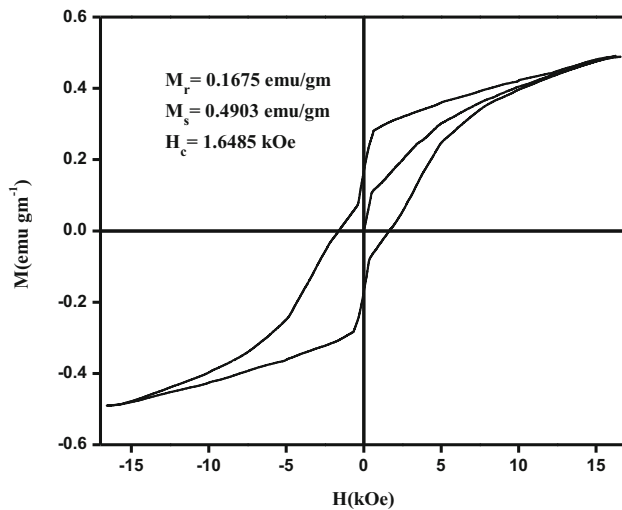


Fig. 14 The M-H loop at ambient condition

evidence of it. The structural distortions from rhombohedral to more unstable trigonal phase have resulted in octahedral tilting. These tiltings reinforce the canting effect and consequently, DM interactions are further assisted [59]. Additionally, the XPS deconvolution of the Fe2p state shows the existence of Fe²⁺ along with the dominant Fe³⁺ state in a comparatively equivalent percentage ratio. This opens up a new possibility of another kind of magnetic interaction, known as the double exchange ferromagnetic mechanism; along Fe²⁺ to Fe³⁺ long/short range chain, via $V^0\bullet$, due to which widened ferromagnetic loop is seen in the experimental loop. Nevertheless, the loop still does not saturate well due to the non-diminishing anti-ferromagnetic signature still having considerable dominance.

4 Conclusion

At last, to put things together, we accumulate our findings as inter-species structural transformations to the R3cH group, which is more unstable than BFO pure phases. This brings structural distortions with it as a consequence of which many physical responses are affected. The mixed symmetric and asymmetric dielectric dispersions are followed in dielectric polarizations, which are again thermally tunable. Clustered dipolar glass-forming nature is verified by the existence of stretched KWW exponentials, which are linked with HN parameters inherently. Dipolar interactions are the dominating factors toward

polarizability, as revealed by the trend of β exponents. The XPS analysis confirms the existence of fluctuating transition ion valency states and adsorbed oxygen defects, which are supposed to be the exchange interaction chain forming ingredients. The study of ferroelectric polarization and magnetization of the formed composite reveals enhanced suppression of space charge leakage and improved opening of M-H loops, reinforced by dual contributing factors such as elevated DM interactions and extension of double exchange chain length. Hence the existence of multiferroic, together with the best possibility of the existence of magneto-electric couplings are ensured. The ac conductivity was found to be best following the phenomenon of carrier tunneling through extended free energy barriers and best fitted following Dyré's formalism. All these findings are quite novel with the compound under investigation, upon which these kinds of analyses were hardly performed before. The above-reported findings may open up a whole new way of looking into the actual behavior of modified BFO, and thereby broaden up its field of applicability.

Author contributions

Conception and design of study: B.N. Parida, Santanu Sen. Acquisition of data: Santanu Sen, R.K. Parida. Analysis and/or interpretation of data: B.N. Parida, Santanu Sen. Drafting the manuscript: Santanu Sen, B.N. Parida. Revising the manuscript critically for important intellectual content: R.K. Parida, B.N. Parida, Santanu Sen. Approval of the version of the manuscript to be published: Santanu Sen, B.N. Parida, R.K. Parida.

Funding

Santanu Sen reports administrative support was provided by Central Institute of Technology Kokrajhar Deemed to be University. Santanu Sen reports administrative support was provided by Central Institute of Technology Kokrajhar Deemed to be University. Santanu Sen reports a relationship with Central Institute of Technology Kokrajhar Deemed to be University that includes: non-financial support.

Data availability

The data acquired in the current study shall be made available on reasonable request.

Declarations

Conflict of interest The authors declare the following financial/personal relationships which may be considered as potential competing interests.

References:

- Kubel, F., Schmid, H. Acta Crystallographica Section B 46, 698–702 (1990) <https://doi.org/10.1107/S0108768190006887>.
- Christian Michel, Jean-Michel Moreau, Gary D. Achenbach, Robert Gerson, W.J. James, (1969) *The atomic structure of BiFeO₃*, Solid State Commun., doi: [https://doi.org/10.1016/0038-1098\(69\)90597-3](https://doi.org/10.1016/0038-1098(69)90597-3).
- James R. Teague, Robert Gerson, W.J. James, *Dielectric hysteresis in single crystal BiFeO₃*, Solid State Communications, Volume 8, Issue 13, 1970, Pp. 1073–1074, [https://doi.org/10.1016/0038-1098\(70\)90262-0](https://doi.org/10.1016/0038-1098(70)90262-0).
- Balesh Kumar Vashisth, Jarnail S. Bangruwa, Anu Beniwal, S.P. Gairola, Ashok Kumar, Nidhi Singh, Vivek Verma, *Modified ferroelectric/magnetic and leakage current density properties of Co and Sm co-doped bismuth ferrites*, Journal of Alloys and Compounds, Volume 698, 2017, Pp. 699–705, <https://doi.org/10.1016/j.jallcom.2016.12.278>.
- Yoshihiro Takahashi, Kousuke Meguro, Hiroshi Naganuma, Nobuaki Terakado, Takumi Fujiwara. *Multiferroic BiFeO₃ - glass-ceramics: Phase formation and physical property Appl. Phys. Lett.* 104, 221901 (2014) <https://doi.org/10.1063/1.4881138>.
- L. Bai, M. Sun, W. Ma, J. Yang, J. Zhang, Y. Liu, Enhanced magnetic properties of Co-Doped BiFeO₃ thin films via structural progression. *Nanomaterials (Basel)*. 10(9), 1798 (2020). <https://doi.org/10.3390/nano10091798>
- Yanhong Gu, Yan Zhou, et al. *Optical and magnetic properties of Smdoped BiFeO₃ nanoparticles around the morphotropic phase boundary region*, AIP Advances 11, 045223 (2021); <https://doi.org/10.1063/5.0042485>
- Jason A. Schiemer, Ray L. Withers, Yun Liu, Michael A. Carpenter, *Ca-Doping of BiFeO₃: The Role of Strain in Determining Coupling between Ferroelectric Displacements, Magnetic Moments, Octahedral Tilting, and Oxygen-Vacancy Ordering*, Chem. Mater. 2013, 25, 21, 4436–4446, 2013 <https://doi.org/10.1021/cm402962q>
- Xia-Li Liang, Jian-Qing Dai, *Prominent ferroelectric properties in Mn-doped BiFeO₃ spin-coated thin films*, Journal of Alloys and Compounds, Volume 886, 2021, 161168, <https://doi.org/10.1016/j.jallcom.2021.161168>.
- Rajasree Das, Gobinda Gopal Khan, Kalyan Mandal, *Pr, and Cr co-doped BiFeO₃ nanotubes: an advance multiferroic oxide material* EPJ Web of Conferences 40, 15015(2013) <https://doi.org/10.1051/epjconf/20134015015>
- Taisan, N.A.; Kumar, S.; Alshoaibi, A. *Structural, Electrical and Optical Properties of TM (Mn and Cr) Doped BiFeO₃ Nanoparticles*, Crystals 2022, 12, 1610. <https://doi.org/10.3390/cryst12111610>
- Priya, A.S.; Geetha, D.; Siqueiros, J.M.; T alu, S, *Molecules* 2022, 27, 7565.
- C M Gokul, Aiswarya Mohan, Soumya G Nair, S R Dhanya, Jyotirmayee Satapathy, *Structural, morphological and thermal analysis of pure and doped (Ho/Nd)-BFO multiferroics*, 2021, *J. Phys.: Conf. Ser.* Doi: <https://doi.org/10.1088/1742-6596/2070/1/012008>
- V. Kumar, S. Singh, Optical and magnetic properties of (1–x)BiFeO₃-xCaTiO₃ nanoparticles. *J. Alloy. Compd.* 732, 350–357 (2018). <https://doi.org/10.1016/j.jallcom.2017.10.236>
- Gomasu Sreenu, Subhadeep Saha, R. N. Bhowmik, J. P. Praveen, Dibakar Das, (2022) *J. Mater. Sci. Mater. Electron.* 33, 24959
- S. Gupta, M. Tomar, V. Gupta, Study on Mn-induced Jahn-Teller distortion in BiFeO₃ thin films. *J. Mater. Sci.* 49, 5997–6006 (2014). <https://doi.org/10.1007/s10853-014-8318-9>
- Kartopu G, Lahmar A, Habouti S (2008) *Observation of structural transitions and Jahn–Teller distortion in LaMnO₃-doped BiFeO₃ thin films*. *Appl Phys Lett* 92:151910(1)–151910(3)
- Muhammad Safwan Sazali, Muhamad Kamil Yaakob, Zakiah Mohamed, Mohamad Hafiz Mamat, Oskar Hasdinor Hassan, Noor Haida Mohd Kaus, Muhd Zu Azhan Yahya, *Chitosan-assisted hydrothermal synthesis of multiferroic BiFeO₃: Effects on structural, magnetic and optical properties*, Results in Physics, 15, 2019, 102740, <https://doi.org/10.1016/j.rinp.2019.102740>.
- S. Wu, J. Zhang, X. Liu, S. Lv, R. Gao, W. Cai, F. Wang, C. Fu, *Nanomaterials* 9(2), 190 (2019). <https://doi.org/10.3390/nano9020190>
- S. Godara, N. Sinha, G. Ray, B. Kumar, Combined structural, electrical, magnetic and optical characterization of bismuth ferrite nanoparticles synthesized by auto-combustion route. *J. Asian Ceram. Soc.* 2(4), 416–421 (2014). <https://doi.org/10.1016/j.jasc.2014.09.001>

21. Rozhin Irandoust, Ahmad Gholizadeh, *A comparative study of the effect of the non-magnetic and magnetic trivalent rare-earth ion substitutions on bismuth ferrite properties: Correlation between the crystal structure and physical properties*, Solid State Sciences, 101, 2020, 106142, <https://doi.org/10.1016/j.solidstatesciences.2020.106142>.
22. Santanu Sen, A. Mondal, R.K. Parida, B.N. Parida, Inorg. Chem. Commun, 2022, doi: <https://doi.org/10.1016/j.inoche.2022.109664>.
23. S. Sen, R.K. Parida, B.N. Parida, Improved multifunctional features in BiFeO₃ solid solution due to partial substitution of MgTiO₃. Appl. Phys. A **128**, 1054 (2022). <https://doi.org/10.1007/s00339-022-06116-5>
24. Pavana S. V. Mocherla, C. Karthik, R. Ubig, M. S. Ramachandra Rao, C. Sudakar (2013) Appl. Phys. Lett. ; <https://doi.org/10.1063/1.4813539>.
25. K. Górska, A. Horzela, Ł Bratek, G. Dattoli, K.A. Penson, J. Phys. A: Math. Theor. **51**, 135202 (2018). <https://doi.org/10.1088/1751-8121/aaafc0>
26. Volkov, A.S., Kuposov, G.D., Perfil'ev, R.O. et al. *Analysis of experimental results by the Havriliak–Negami model in dielectric spectroscopy*, Opt. Spectrosc. **124**, 202–205 (2018). <https://doi.org/10.1134/S0030400X18020200>
27. Yu. I. Yurasov, A. V. Nazarenko *Parameter of dielectric loss distribution in the new model for complex conductivity based on Havriliak–Negami formula*, (2020), journal of advanced dielectrics Vol. 10, Nos. 1 & 2 2060006 (8 pages) DOI: <https://doi.org/10.1142/S2010135X20600061>
28. R. Casalini, CM. Roland, (2003) Phys. Rev. Lett. 91 015702
29. K. Fukao, Y. Miyamoto *Glass transitions, and dynamics in thin polymer films: Dielectric relaxation of thin films of polystyrene* Phys. Rev. E, 2000, 61, 1743 <https://doi.org/10.1103/PhysRevE.61.1743>.
30. R. Casalini, C.M. Roland, Aging of a low molecular weight poly(methyl methacrylate). J. Non-Cryst. Solids **357**(2), 282–285 (2011). <https://doi.org/10.1016/j.jnoncrysol.2010.07.048>
31. F. Alvarez, A. Alegria, and J. Colmenero *Relationship between the time-domain Kohlrausch-Williams-Watts and frequency-domain Havriliak-Negami relaxation functions*, Phys. Rev. B (1991), 44, 7306, <https://doi.org/10.1103/PhysRevB.44.7306>.
32. F. Alvarez, A. Alegria, J. Colmenero Phys. Rev. B **47**, 125 (1993). <https://doi.org/10.1103/PhysRevB.47.125>
33. A.A. Bokov, M. Maglione, Z.-G. Ye, J. Phys.: Condens. Matter (2007). <https://doi.org/10.1088/0953-8984/19/9/092001>
34. R. Bergman, General susceptibility functions for relaxations in disordered systems. J. Appl. Phys. **88**, 1356 (2000). <https://doi.org/10.1063/1.373824>
35. A. A. Bokov, Z.-G. Ye *Double freezing of dielectric response in relaxor Pb(Mg_{1/3}Nb_{2/3})O₃ crystals*, Phys. Rev. B (2006) 74, 132102 <https://doi.org/10.1103/PhysRevB.74.132102>.
36. T. Prakash, K. Padma Prasad, R. Kavitha, S. Ramasamy, (2007) Journal of Applied Physics 102, 104104
37. Santanu Sen, R.K. Parida, B.N. Parida, (2023) Phys. B Cond. Mat, doi: <https://doi.org/10.1016/j.physb.2022.414559>.
38. S. Mohanty, S. Behera, Santanu Sen, B. N. Parida, Rashmi Singh, *Dielectric, optical, and magnetic behaviors of magnesium iron-based double perovskite*, 2022 ECS J. Solid State Sci. Technol. 11 113003, DOI <https://doi.org/10.1149/2162-8777/ac9ff1>.
39. S. Mohanty, S. Sen, S. Behera et al., J. Mater. Sci: Mater. Electron. **33**, 23770–23780 (2022). <https://doi.org/10.1007/s10854-022-09135-3>
40. Sonali Saha and T. P. Sinha *Low-temperature scaling behavior of BaFe_{0.5}Nb_{0.5}O₃* Phys. Rev. B(2002) 65, 134103.
41. K.P. Padmasree, D.K. Kanchan, A.R. Kulkarni, Solid State Ionics (2006). <https://doi.org/10.1016/j.ssi.2005.12.019>
42. Y. Barsukov, J.R. Macdonald, Electrochemical impedance spectroscopy. Charact. Mater. (2012). <https://doi.org/10.1002/0471266965.com124>
43. C. Ruttanapun, S. Maensiri, J. Phys. D Appl. Phys. **48**, 495103 (2015). <https://doi.org/10.1088/0022-3727/48/49/495103>
44. J. Morales, L. Saánchez, F. Martíin, F. Berry, X. Ren, F.D.P.M. Jiménez, *Synthesis and characterization of nanometric iron and iron-titanium oxides by mechanical milling*. J. Electrochem. Soc. **152**(9), A1748–A1754 (2005)
45. W. Choi, H.-C. Shin, J.M. Kim, J.-Y. Choi, W.-S. Yoon, J. Electrochem. Sci. Technol. **11**, 1–13 (2020)
46. K. Shimakawa, Electrical Transport Properties of Glass, in *Springer Handbook of Glass*. (Springer, Berlin/Heidelberg, Germany, 2019), p.343
47. S.S. Batool, Z. Imran, K. Rasool et al., Sci. Rep. **10**, 2775 (2020). <https://doi.org/10.1038/s41598-020-59563-6>
48. L. Zhang, F. Liu, K. Brinkman, K.L. Reifsnider, A.V. Virkar, A study of gadolinia-doped ceria electrolyte by electrochemical impedance spectroscopy. J. Power Sources **247**, 947–960 (2014). <https://doi.org/10.1016/j.jpowsour.2013.09.036>
49. Yu. Shenglong, H. Bi, J. Sun, L. Zhu, Yu. Huamin, Lu. Chunling, X. Liu, Effect of grain size on the electrical properties of strontium and magnesium doped lanthanum gallate electrolytes. J. Alloy. Compd. **777**, 244–251 (2019). <https://doi.org/10.1016/j.jallcom.2018.10.257>
50. C. Jeppe, Dyre The random free-energy barrier model for ac conduction in disordered solids Journal of Citation. J. Appl. Phys. **64**, 2456 (1988). <https://doi.org/10.1063/1.341681>

51. S. Flügge (Ed.), *Handbuch der Physik*, Band 20, Springer, Berlin (1957), Vol. 20, p. 350.
52. H. E. Taylor, *J. Soc. Glass Technol.* **41**, 3S0T (1957); *ibid.* **43**, J24T (1959).
53. R. Gupta, J. Shah, S. Chaudhary et al., Magnetolectric coupling-induced anisotropy in multiferroic nanocomposite $(1-x)\text{BiFeO}_3-x\text{BaTiO}_3$. *J Nanopart Res* **15**, 2004 (2013). <https://doi.org/10.1007/s11051-013-2004-8>
54. S. Dash, R.N.P. Choudhary, P.R. Das et al., Effect of KNbO_3 modification on structural, electrical and magnetic properties of BiFeO_3 . *Appl. Phys. A* **118**, 1023–1031 (2015). <https://doi.org/10.1007/s00339-014-8862-9>
55. Anshu Sharma, R.K. Kotnala, N.S. Negi, (2014) *J. Alloys Comp.*, **582**, 628–634, <https://doi.org/10.1016/j.jallcom.2013.08.087>.
56. S. Jangra, S. Sanghi, A. Agarwal, M. Rangi, K. Kaswan, S. Khasa, Improved structural, dielectric and magnetic properties of Ca^{2+} and Nb^{5+} co-substituted BiFeO_3 multiferroics. *J. Alloy. Compd.* **722**, 606–616 (2017). <https://doi.org/10.1016/j.jallcom.2017.06.132>
57. A. Mukherjee, M. Banerjee, S. Basu, Nguyen Thi Kim Thanh, L.A.W. Green, M. Pal, (2014) *Phys. B Condens Mat.*, **448**, 199–203
58. G. Catalan, J.F. Scott, *Phys. Appli. Bismuth Ferrite* (2009). <https://doi.org/10.1002/adma.200802849>
59. Marzouk, Mostafa., Hashem, Hany., Soltan, Soltan., Ramadan, A. J. *Mater. Sci. Mater. Electron*, 2020, doi: <https://doi.org/10.1007/s10854-020-03126-y>.
60. C. Ederer, N.A. Spaldin, *Phys. Rev. B* (2005). <https://doi.org/10.1103/PhysRevB.71.060401>
61. N. Maso, A. West, Electrical properties of Ca-doped BiFeO_3 ceramics: from p-type semiconduction to oxide-ion conduction. *Chem. Mater Chem. Mater.* **24**(11), 2127–2132 (2012). <https://doi.org/10.1021/cm300683e>
62. T. Moriya, *Magnetism* (Academic, New York, 1963)
63. I.E. Dzyaloshinski, *J. Phys. Chem. Solids* **4**, 241 (1958)
64. B. Khan, M.K. Singh, P. Yadav, A. Kumar, G. Singh, P. Kumar, *Mater. Chem. Phys* **290**, 126642 (2022). <https://doi.org/10.1016/j.matchemphys.2022.126642>
65. Q.Q. Wang, Z. Wang, X.Q. Liu, X.M. Chen, Improved structure stability and multiferroic characteristics in CaTiO_3 -modified BiFeO_3 ceramics. *J. Am. Ceram. Soc.* **95**(2), 670–675 (2011). <https://doi.org/10.1111/j.1551-2916.2011.04824.x>

Publisher's Note Springer Nature remains neutral with regard to jurisdictional claims in published maps and institutional affiliations.

Springer Nature or its licensor (e.g. a society or other partner) holds exclusive rights to this article under a publishing agreement with the author(s) or other rightsholder(s); author self-archiving of the accepted manuscript version of this article is solely governed by the terms of such publishing agreement and applicable law.